

Experimental and numerical analysis of the effect of temperature on the mode I and mode II delamination of glass fiber woven composites

Arouche, Marcio Moreira; Pavlovic, Marko

DOI

[10.1016/j.compositesb.2025.112131](https://doi.org/10.1016/j.compositesb.2025.112131)

Publication date

2025

Document Version

Final published version

Published in

Composites Part B: Engineering

Citation (APA)

Arouche, M. M., & Pavlovic, M. (2025). Experimental and numerical analysis of the effect of temperature on the mode I and mode II delamination of glass fiber woven composites. *Composites Part B: Engineering*, 293, Article 112131. <https://doi.org/10.1016/j.compositesb.2025.112131>

Important note

To cite this publication, please use the final published version (if applicable). Please check the document version above.

Copyright

Other than for strictly personal use, it is not permitted to download, forward or distribute the text or part of it, without the consent of the author(s) and/or copyright holder(s), unless the work is under an open content license such as Creative Commons.

Takedown policy

Please contact us and provide details if you believe this document breaches copyrights. We will remove access to the work immediately and investigate your claim.



Experimental and numerical analysis of the effect of temperature on the mode I and mode II delamination of glass fiber woven composites

Marcio Moreira Arouche ^{*} , Marko Pavlovic

Faculty of Civil Engineering and Geosciences, Delft University of Technology, Stevinweg 1, 2628 CN, Delft, Netherlands

ARTICLE INFO

Handling Editor: Prof. Ole Thomsen

Keywords:

Polymer-matrix composites
Delamination
Fracture tests
Temperature effects
Failure mechanisms
Cohesive zone modelling (CZM)

ABSTRACT

This work focuses on investigating the effect of short-term changes of temperature on the mode I and mode II glass fibers woven composite interleaved with layers of chopped strand mat (CSM). Existing experimental and numerical methods are critically applied to characterize and model the delamination of the woven-CSM composite laminate. Double cantilever beam (DCB) and end notched flexure (ENF) tests are performed in non-post cured and post cured specimens at room temperature (21 °C), and the operational conditions are investigated on post cured specimens tested in low (−10 °C) and high (70 °C) temperatures. The fracture behavior is characterized using the compliance-based beam method (CBBM) while crack length estimations based on the specimen compliance are compared to direct measurements from digital image correlation (DIC). Then, a failure analysis was performed using an optical profilometer and scanning electron microscopy (SEM). Temperature changes affected the preferential crack path for the woven composite delamination in mode I loading conditions. However, the crack path in mode II fracture remained independent of the testing temperature. Fractography results revealed temperature-dependent failure mechanisms, with an increase of fiber/matrix interface debonding and matrix deformation in higher temperatures. The higher matrix ductility translated into an improvement of the delamination fracture toughness in both mode I and mode II loading conditions. Finally, non-linear cohesive models directly derived from experimental results were capable to accurately reproduce the mode I and mode II delamination fracture behavior of the woven-CSM composite in different temperatures.

1. Introduction

Fiber-reinforced polymers (FRPs) are increasingly popular in structural applications due to their excellent strength-to-weight ratio and design flexibility. These composite materials are manufactured using long fiber plies stacked together with a polymeric resin matrix. Novel materials, manufacturing processes and lay-up designs have been introduced as extensive research is required to evaluate and identify the best possible combination of parameters to optimize the performance of composite structures for real-life applications [1]. To achieve this goal, it is fundamental to understand the relationship between material, mechanical properties and environmental effects.

Several methods have been developed to characterize the mechanical properties of composite materials under delamination. It assumes that the structure is not continuous, considering manufacturing imperfections or any damage caused during operational life. These imperfections are often regions of stress concentration, and, therefore, initiation points for a crack to initiate, propagate and cause failure of the

structure [2]. The fracture mechanics approach assumes that a crack develops in one or a combination of three different loading modes: opening, or mode I; in-plane shear, or mode II; and out-of-plane shear, or mode III. Analytical methods based on fracture mechanics are reliable and straight-forward but limited to simple geometries.

The pure mode I fracture of composite materials is usually characterized by the double cantilever beam (DCB) test. In pure mode II fracture conditions, the end notched flexure (ENF) test is the most common method. In these tests, the fracture toughness can be defined by the energy release rate (ERR) and calculated from analytical methods based on linear elastic fracture mechanics [2]. In particular, the method proposed by De Moura et al. [3,4], the compliance-based beam method (CBBM), allows calculating the mode I and mode II fracture toughness of a specimen directly from experiments. The CBBM estimates the crack length and the elastic modulus of the material based on the specimen compliance (δ/P) and test geometry. Therefore, it is expected to implicitly accounts for the fracture process zone (FPZ) and changes in the material properties.

^{*} Corresponding author.

E-mail addresses: m.moreiraarouche@tudelft.nl (M.M. Arouche), m.pavlovic@tudelft.nl (M. Pavlovic).

<https://doi.org/10.1016/j.compositesb.2025.112131>

Received 3 October 2024; Received in revised form 11 December 2024; Accepted 5 January 2025

Available online 8 January 2025

1359-8368/© 2025 The Authors. Published by Elsevier Ltd. This is an open access article under the CC BY license (<http://creativecommons.org/licenses/by/4.0/>).

For structural design, the flexibility of finite element modelling (FEM) presents more appropriate solutions. In particular, damage modelling is still an innovative field under intense development [1]. The damage mechanics approach is applied to model the ductile behavior of a composite delamination. In the cohesive zone modelling (CZM), a relationship between the traction and separation of two surfaces is implemented in FEM, allowing the prediction of the performance of structures with complex geometries. Several works addressed the cohesive behavior of bonded interfaces in mode I fracture [5–7]. Pereira et al. [5] obtained consistent results of a fracture in a bovine cortical bone tissue using both direct and inverse methods. The direct method consists of a differentiation of the relationship between the fracture energy and the crack tip opening displacement, monitored by video extensometers or digital image correlation (DIC) technique. The inverse method is based on a calibration of the CZM with an optimization algorithm of the numerical results. Although the shape of the traction-separation function was different, both methods produced similar global responses from experiments. Huo et al. [6] showed the correlation between the global loading response from DCB tests and the local displacements of ductile adhesive interface. The shape of the damage evolution curve was accurately modelled with DIC and verified with experimental results. Moreover, the experimental study performed by Gorman and Thouless [7] in steel bonded DCB specimens showed that the magnitude of the cohesive behavior measured with DIC is consistent with the analytical predictions based on linear elastic fracture mechanics (LEFM). Application of the direct method leading to derivation of non-linear traction separation laws of the cohesive zone models is common for mode I behavior but less implemented so far for the mode II due to difficulty of accurately determining the crack tip slip displacement.

Azevedo et al. [8] investigated the mode II shear fracture of adhesively bonded joints between high-strength aluminium adherends. They estimated the shear fracture behavior by a curve fitting procedure to a bilinear cohesive law. Ouyang and Li [9] investigated interface fracture behavior of adhesive joints using ENF tests with varied initial crack length. They compared different traction-separation functions and observed that, unlike the mode I fracture, the shape of the cohesive law becomes relatively important under shear loading conditions. Fernandes et al. [10] investigated the mode II cohesive behavior from unidirectional carbon-epoxy composite bonded joints using ENF tests. They derived a non-linear traction-separation function directly from the experiments and successfully adjusted it to a trapezoidal shape. Arouche et al. [11] showed the use of a layer of glass fiber chopped strand mat as a toughening mechanism to improve the performance of composite structures. These studies are applied to the characterization of bonded interfaces and can be generally extended to composite delamination. However, the complex failure mechanisms of composite materials must also be considered.

The type of material and composite lay-up shows a major effect on the mechanical behavior of composite structures [1]. De Baere et al. [12] investigated the mode I and mode II interlaminar fracture of carbon fabric composites with a weaving pattern using DCB and ENF tests. They showed the consistency of analytical models based on LEFM to calculate the fracture toughness of laminates with woven plies. The cohesive behavior of unidirectional fiber composites with extensive fiber bridging were successfully calibrated by Höwer et al. [13] from experiments with DIC in mode I, mode II and mixed-mode loading conditions. The development of new lay-up designs with optimized mechanical properties is fundamental to the expansion of the composite materials technology.

Several authors have suggested the use of interleaved laminates to improve the delamination fracture toughness of composites [14–18]. An early study obtained significant toughening effect of a carbon fiber composite by using thick adhesive interleaves [14]. Saghafi et al. [15] investigated combinations of interleaved composite nanofibrous mats in unidirectional glass/epoxy laminates. They showed a significant

improvement of the ERR, particularly in mode II condition. Zheng et al. [16] also used sandwiched layers of modified polymers to increase both mode I and mode II interlaminar toughness of carbon fiber composites. Idrees et al. [17] showed a strongly influence of the resin properties and resin rich layers in the achievable fracture toughness of interleaved woven glass fiber laminates. Moreover, the work of Hosseini et al. [18] revealed that the presence of a mat interlayer can also reduce the delamination fracture properties compared to the composite without mat. They pointed out that the dominant mechanism to increase the mode II fracture toughness is related to the fiber-matrix interface interaction. These experimental works addressed the delamination failure mechanisms at microscopic scale to present insight on the mechanical behavior obtained from fracture tests in coupon specimens. However, the correlation of experimental analysis and numerical modelling is still required to the development of primary structural applications of composite materials.

Understanding the effect of environmental conditions on composite materials is a fundamental aspect for ensuring the structural integrity. In particular, short-term changes of temperature have a significant effect on the delamination of unidirectional fiber composites [19–23]. Fernandes et al. [19] investigated the mode I and mode II fracture of carbon-epoxy bonded joints between 0 and 50 °C. The cohesive behavior was derived from a numerical fitting of experimental results using a trapezoidal function. Although this inverse approach is able to capture the global changes of the mechanical behavior of the specimens, it is not able to account for the physical changes in the material failure caused by the different conditions of temperature. Ibrahim and Albarbar [20] carried out a numerical study to address the effect of temperature on the CZM of a composite delamination. They detected the development of underlying toughening mechanisms in the damage initiation at cryogenic conditions. Low temperatures tend to slightly increase the longitudinal elastic modulus and strength of structural composites [23].

Cao et al. [21] investigated the effect of temperatures on the cohesive behavior in mode I delamination using a trilinear function. They expressed a temperature-dependent CZM based on a trilinear model from Mohammadi et al. [24]. Their work showed that temperature affected the damage onset and critical opening displacements, as well as the bridging traction. Denser fiber bridging and higher bridging traction were observed with a more ductile matrix fracture at higher temperatures. The temperature effect on the elastic properties of the composite needs to be considered to guarantee model accuracy. A temperature-dependent elastic modulus was proposed by Mivehchi and Varvani-Farahani [25] to model the delamination process at an arbitrary temperature.

Machado et al. [22] observed an increase of the mode II fracture toughness of composite laminates with the increase of temperatures. They obtained good agreement with the global response between numerical models and experiments using bilinear cohesive functions estimated from the onset of delamination initiation and propagation. Changes on the cohesive behavior of a composite delamination in different temperatures are usually attributed to the embrittlement of the resin matrix. Generally, this effect is modelled by calibration of experimental results using simplified functions of the traction-separation relationship. However, the underlying mechanisms of the composite delamination of the composite material remain unclear. When considering the complex delamination behavior of real-application composite lay-ups, a reliable prediction of the effect of temperature is fundamental for the implementation of new technologies.

In the construction sector, the wrapped composite joints have been developed as an alternative to welding for connecting steel circular hollow sections [26]. This new technology promises to increase the life-time and reduce the weight of the structure. The composite wrap is designed for high mechanical performance, using a vinyl ester polymer matrix and woven glass fibers interleaved with chopped strand mat. In such configuration, predicting the mechanical behavior of the material in operational conditions is critical to the design and implementation of

the technology. This requires the investigation of reliable analytical and numerical methods to characterize the composite delamination under both mode I and mode II fracture conditions.

This work investigates the effect of operational conditions of temperature on the composite material used in the wrapped composite joints. Existing experimental and numerical methods was critically applied to characterize and model the delamination of woven-CSM composite laminates. DCB and ENF tests are performed to characterize the mode I and mode II fracture in non-post cured and post cured specimens in room temperature (21 °C), and post cured specimens in low (−10 °C) and high (70 °C) temperatures. Crack length estimations based on the specimen compliance are compared to direct measurements from DIC, and the mode I and mode II ERR are calculated using the CBBM. Then, temperature-dependent failure mechanisms are interpreted by a detailed fractographic analysis. Finally, non-linear cohesive models of the delamination crack are developed directly from experimental results and implemented in FEM to predict the mechanical responses under different temperatures.

2. Experimental method

2.1. Manufacturing of specimens

A glass fiber reinforced polymer (GFRP) composite plate was manufactured. A vinyl ester resin was applied to the hand lay-up lamination of glass fiber bi-directional woven plies interleaved with chopped strand mat (CSM), as shown in Fig. 1. A non-adhesive Teflon insert of 32 μm thickness was placed at the mid-plane to create an artificial pre-crack. The laminated plate cured in air conditions of 18 ± 1 °C and 50 ± 5 % humidity. Then, the composite plate was cut to coupon specimens using water jet. A single specimen geometry was designed for both DCB and ENF tests. The woven fibers remain in the direction of the pre-crack and perpendicular. Finally, part of the specimens was post cured in an oven at 120 °C for 7 h. The testing specimens have a nominal length of 230 mm, and an average width (w) and thickness (2h) of 19.68 ± 0.14 mm and 7.68 ± 0.21 mm, respectively, measured from the average of 3 different sections using a digital caliper. The chosen specimen geometry allows testing the composite delamination in both mode I and the mode II fracture conditions. Material properties of the composite laminate were obtained in a previous work [27].

2.2. Dynamic mechanical analysis

A dynamic mechanical analysis (DMA) was carried out on non-post cured and post cured specimens to check the curing condition of the composite material. Samples were heated from 25 to 175 °C at a constant rate of 5 °C/min while a torsion vibration of 1 Hz was applied, in accordance with standard ISO 6721-11 [28]. Fig. 2 shows the storage modulus (decreasing curve) and damping factor (increasing curve) resulted from the DMA of 3 samples tested in each condition. The glass transition temperature (T_g) was obtained from the onset point of the storage modulus. In non-post cured specimens, the T_g is obtained from

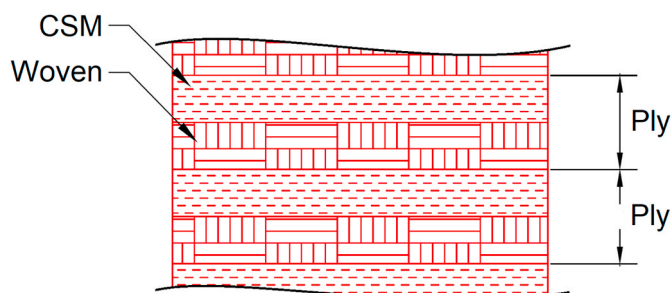


Fig. 1. Lay-up scheme of the composite specimens.

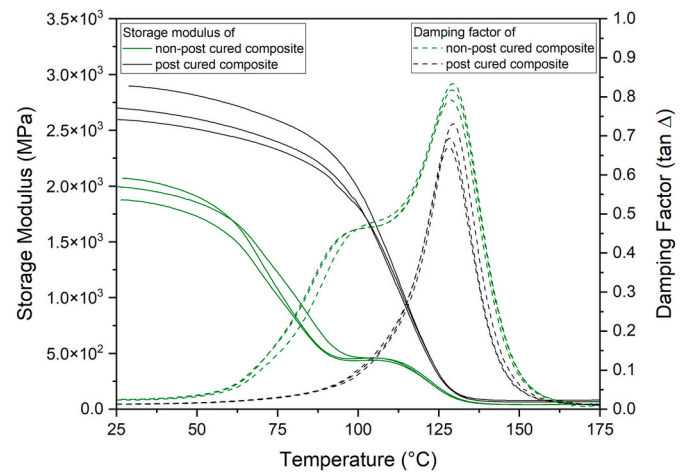


Fig. 2. DMA curves.

the first slope of the storage modulus curve, that represents the transition from a glassy to a rubbery state. The second slope is relative to the post curing of the sample during the DMA. In the case of fully post cured specimens, only one slope is developed during the heating process, meaning that the material is fully cured. The average T_g of 68 ± 2 °C and 111 ± 2 °C were obtained for the non-post cured and post cured specimens, respectively.

2.3. Fracture tests

A thin layer of white matt paint was coated and a random black speckle pattern was applied to the measurement surface of the specimen. A high resolution camera (50.6 MPx) and a blue LED light source were positioned to the measurement surface to acquire the full field displacements by DIC. Photos were synchronized with load measurements from the testing machine. For the image processing, surface points were recognized by a small neighborhood of a square with a side length of 19 pixels and a step size of 11 pixels set in the DIC software.

DCB and ENF tests were performed to evaluate the effect of temperature on the mode I and mode II fracture delamination of the composite material. Experiments were carried out in an universal testing machine coupled with a 15 kN load cell. Table 1 shows the test matrix. Non-post cured (NPC) and post cured (PC) specimens were tested at the room temperature (RT) of 21 ± 1 °C. In addition, a climate chamber was used with the test set up for testing post cured specimens in the low temperature (LT) of −10 ± 1 °C and the high temperature (HT) of 70 ± 1 °C. Two air mixing fans improved stability of air conditions over time and the specimens were maintained in a constant condition for 7 h prior to the tests to ensure a homogeneous temperature field in the material. Series of 5 specimens were tested in each configuration in order to obtain a statistically representative average of the material behavior.

2.3.1. DCB tests

In order to transfer the loads during the DCB tests, loading blocks

Table 1
Test matrix.

Test series	Set up	Post curing	Testing temperature (°C)	Number of tests
DCB-NPC	DCB	no	21	5
DCB-PC	DCB	yes	21	5
DCB-LT	DCB	yes	−10	5
DCB-HT	DCB	yes	70	5
ENF-NPC	ENF	no	21	5
ENF-PC	ENF	yes	21	5
ENF-LT	ENF	yes	−10	5
ENF-HT	ENF	yes	70	5

were bonded to the specimens. Fig. 3 shows the DCB test scheme (Fig. 3a) and a photo of the test set up (Fig. 3b). The testing procedure was defined based on the specifications of ASTM D5528 [29] although the woven-CSM laminate evaluated in this work is not specifically addressed in the standard. Specimens have relatively thicker plies than typically described in the standard (3–5 mm) due to the relatively thicker plies of the hand lay-up composite material. During the tests, an opening load P is applied to the specimen in a constant crosshead displacement of 1 mm/min while DIC photos were taken at the frequency of 0.33 Hz in the region of crack initiation and 0.10 Hz after crack propagation.

2.3.2. ENF tests

The ENF testing procedure was defined based on the specifications of ASTM D7905 [30] although the woven-CSM laminate evaluated in this work is not specifically addressed in the standard. The standardized test span of 100 mm was set and the specimens were positioned to have an initial crack length of 30 mm. During the tests, a compressive load P is applied to the half-span specimen in a constant crosshead displacement of 0.5 mm/min while photos were taken at the frequency of 0.33 Hz. The ENF test scheme is presented in Fig. 4a and a photo of the test set up is shown in Fig. 4b.

3. Data reduction method

The delamination fracture toughness is determined by the ERR, or fracture energy (G), for a crack growth. In a tested specimen, it can be analytically derived from Irwin-Kies equation:

$$G = \frac{P^2}{2B} \frac{dC}{da} \quad (1)$$

where P is the applied load, B is the specimen width, C is the specimen compliance, or the ratio of the load point displacement to the applied load ($C = \delta/P$), and a is the crack length. The compliance-based beam method (CBBM) [3,4] relates Timoshenko beam theory and the specimen compliance to obtain the fracture energy. For a DCB test set up, it

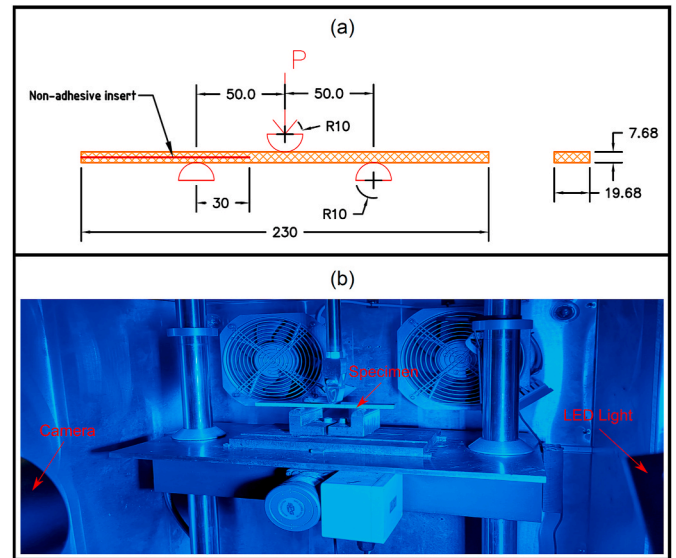


Fig. 4. ENF test scheme and set up (dimensions in millimeters).

gives:

$$C_{(DCB)} = \frac{8a^3}{E_f B h^3} + \frac{12a}{5G_{13} B h} \quad (2)$$

where h is the specimen half thickness, E_f is the flexural modulus and G_{13} is the interlaminar shear modulus. Equations (1) and (2) can be combined to obtain the mode I fracture energy, G_I :

$$G_I = \frac{6P^2}{B^2 h} \left(\frac{2a^2}{h^2 E_f} + \frac{1}{5G_{13}} \right) \quad (3)$$

The flexural modulus, E_f , of each specimen can be obtained from Equation (4) using the measured initial compliance in the linear region, C_0 , and the corrected initial crack length ($a_0 + \Delta$) proposed by Ref. [31] and given as:

$$E_{f(DCB)} = \left(C_0 - \frac{12(a_0 + \Delta)}{5BhG_{13}} \right)^{-1} \frac{8(a_0 + \Delta)^3}{Bh^3} \quad (4)$$

Where Δ is a correction for root rotation effect at the crack tip:

$$\Delta = h \left(\frac{E_f}{11G_{13}} \left[3 - 2 \left(\frac{\Gamma}{1 + \Gamma} \right)^2 \right] \right)^{1/2} \quad (5)$$

And:

$$\Gamma = 1.18 \frac{(E_f E_3)}{G_{13}} \quad (6)$$

Where E_3 is the transverse elastic modulus. An iterative procedure should be done between Equations (4) and (5) in order to obtain a converged value for E_f . Nominal values of 5.0 GPa and 3.5 GPa were taken from previous works [27,32] for E_3 and G_{13} , respectively. Experimental determination of these parameters is not needed since realistic differences in these values do not have significant impact on the calculation of the fracture energy.

Generally, the crack length measurement during the tests requires the use of a detection technique and data processing. Alternatively, the CBBM provides a straight-forward estimation of the crack length as function of the specimen compliance during the test. An equivalent crack length, $a_{e(DCB)}$, is obtained from Equation (2) for DCB tests.

In the case of an ENF test set up, the specimen compliance becomes:

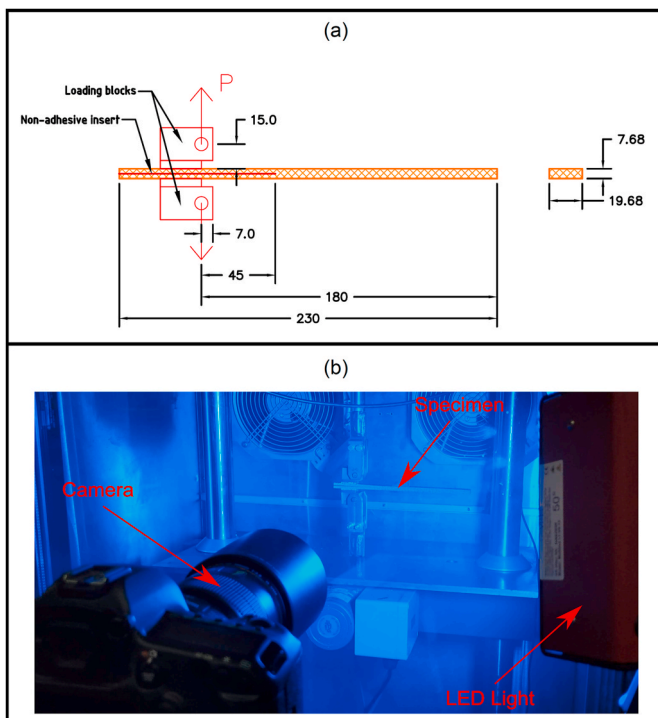


Fig. 3. DCB test scheme and set up (dimensions in millimeters).

$$C_{(ENF)} = \frac{3a^3 + 2L^3}{8E_f Bh^3} + \frac{3L}{10G_{13} Bh} \quad (7)$$

where L is the half span of the ENF test. Combining Equations (1) and (7), the mode II fracture toughness, G_{II} , can be obtained:

$$G_{II} = \frac{9P^2 a^2}{16B^2 h^3 E_f} \quad (8)$$

The flexural modulus, E_f , can be estimated experimentally, for each ENF test specimen, using the initial compliance C_0 and the initial crack length a_0 , as shown in Equation (9):

$$E_{f(ENF)} = \frac{3a_0^3 + 2L^3}{8Bh^3 C_{0corr}} \quad (9)$$

Where:

$$C_{0corr} = C_0 - \frac{3L}{10G_{13} Bh} \quad (10)$$

Finally, the equivalent crack length of an ENF test, $a_{e(ENF)}$, can be obtained directly from Equation (11):

$$a_{e(ENF)} = \left[\frac{1}{3} \left(\left(C - \frac{3L}{10G_{13} Bh} \right) 8E_f Bh^3 - 2L^3 \right) \right]^{1/3} \quad (11)$$

The CBBM allows accounting for the variability of the material properties between different specimens and testing conditions. The estimation of an equivalent crack length should consider the energy dissipated by the FPZ that affects the specimen compliance.

4. Experimental analysis

4.1. Crack length measurements

The crack length was measured by DIC. The DIC technique provides full-field displacements of a target object by correlating local features on images recorded at reference and deformed configurations based on a suitable textured pattern. The crack opening displacement (COD) was measured from sections of every 1 mm step along the crack path, as shown in Fig. 5. For clarity, only a few COD curves are presented in the graphs. The distance between upper and lower measurements remained

around 1.3 mm, large enough to avoid the lost of surface component near the crack due to high deformations of the measurement surface, and short enough to avoid any significant contribution of the geometrical non-linearity of the arms. In fact, a preliminary analysis showed that the position of the measurement points has negligible influence on the measured COD.

The COD obtained from DCB tests (Fig. 5a) showed a consistent profile, that can be typically described as a region of negligible COD, that defines an uncracked interface, followed by a region of negative COD, where compressive stresses are present, and a region of sharp increase of COD, which defines the presence of a crack. In the case of the ENF tests (Fig. 5b), the region of compressive stresses is also present although less evident due the pure shear configuration. Therefore, the location of the crack tip in defined in both tests as the point where the COD becomes positive after compression.

Representative load-displacement-crack length curves are presented in Fig. 6. The displacement of DCB tests obtained from the machine crosshead was corrected to remove typical non-linearities exhibited during initial specimen loading due to load fixture or specimen seating [29]. Therefore, displacement values shown in the DCB test cure in 6a are shifted such that the linear fit to the initial part of each curve passes through the origin. In the case of ENF tests (Fig. 6b), displacements were obtained from DIC measurements of vertical displacement of the load application point minus the average vertical displacement of the support points identified on the specimen. This allows removing effects of non-linearities of the testing system from the compliance measurements. ENF load-displacement curves showed stable crack development followed by a sudden drop after reaching peak load.

Crack length measurements were obtained for DCB and ENF tests by the equivalent crack length estimated from the specimen compliance and the DIC-based method. A comparison between the two methods shows that the compliance-based method gives more conservative measurements than the direct measurements of the COD. In addition, the compliance-based measurements are not able to capture the crack initiation in either DCB or ENF tests. Identification of stress concentrations ahead of the crack tip in early stages of the crack development requires external measuring techniques. Instead, the CBBM relies on the global mechanical behavior of the specimen.

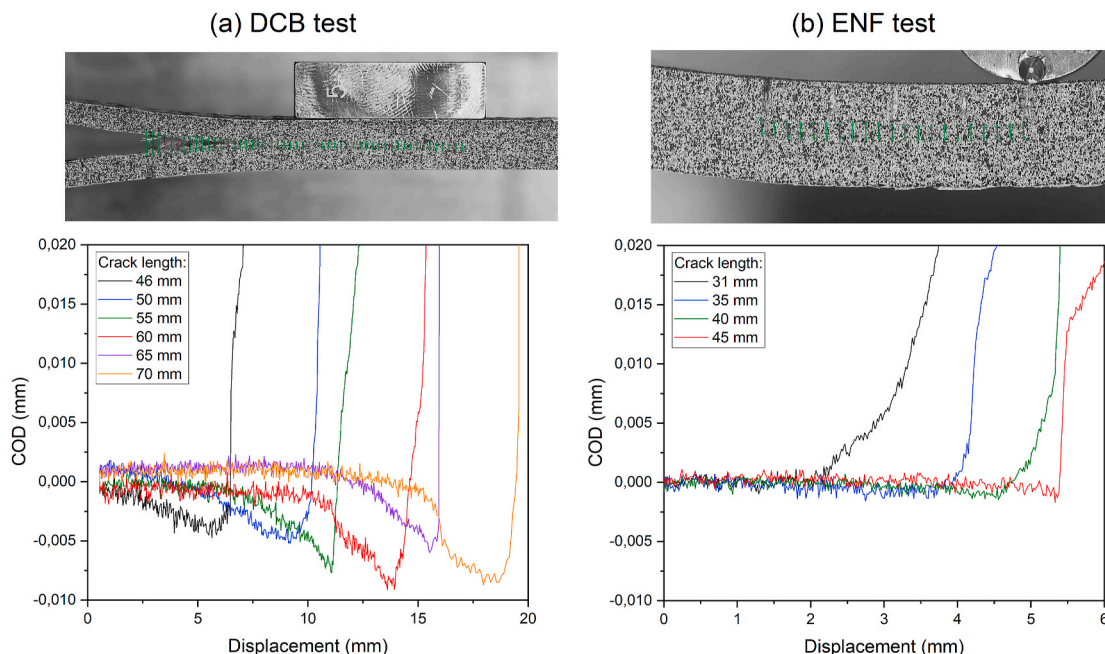


Fig. 5. Crack length measurement of (a) DCB and (b) ENF tests by DIC.

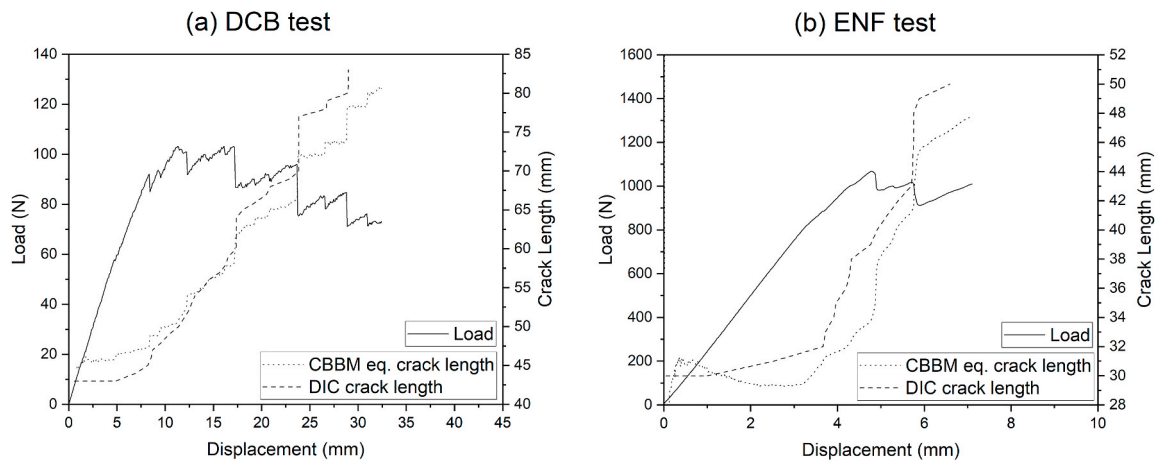


Fig. 6. Comparison between crack length measurements with DIC and equivalent crack length from CBBM in representative (a) DCB and (b) ENF tests.

4.2. Fracture toughness

The Resistance-curves, or R-curves, are applied to characterize the interlaminar fracture toughness of the composite laminate. The R-curves were determined directly from experiments using the CBBM, as described in section 3, and from DIC crack length measurements. Equation (3) was applied to the calculation of the mode I fracture energy (G_I) in the DCB tests, and the mode II fracture energy (G_{II}) was calculated in the ENF tests using Equation (8). The initial compliance of the specimen (C_0) was taken as the local minimum compliance after the initial non-linearity of the test.

The R-curves obtained using the CBBM and the DIC-based crack length measurements are compared in Fig. 7 using representative results from DCB and ENF tests. Results show that the compliance-based measurements are not able to properly identify the crack initiation in either of the tested methods. This is particularly observed in DCB tests (Fig. 7a), where the first 2.5 mm of crack growth (Δa , Δa_e) was not captured from the CBBM. In fact, identification of stress concentrations ahead of the crack tip and therefore consistent measurement of crack initiation of woven-CSM composites is challenging even with the support of external measuring techniques and give scatter results due to the heterogeneous nature of the material. However, both curves overlap as the crack fully develops, allowing for a reliable measurement of the fracture toughness based only on the experimental compliance of the test specimen. Therefore, the CBBM will be used hereafter for the

analysis of post curing and temperature effects.

The mode I R-curves are presented in Fig. 8 for the different testing series. Non-post cured specimens presented consistent mechanical behavior, as shown in Fig. 8a. The same can be stated for post cured specimens tested in 21 °C and -10 °C, as shown in Fig. 8b and c, respectively. However, specimens tested in 70 °C, in Fig. 8d, presented more scattered results. The reason for this behavior in high temperature will be discussed afterwards. In general, each curve reveals an initial increase in fracture energy, defined as the formation of an extensive FPZ until the crack is fully developed. This effect is explained by the deformation and cracking of the resin matrix and the large fiber bridging in opening loading conditions. Then, the plateau region of crack propagation exhibited “stick-slip” crack growth behavior, typical from the delamination mechanism in woven fiber composites [12]. This type of crack propagation can be separated by periods of crack initiation (high peaks) and arrest (low peaks). This behavior remains in different temperature conditions, although the peaks are more pronounced in high temperature and less in low temperature.

The critical mode I fracture energy, G_{Ic} , is the plateau of the DCB R-curves calculated as the average fracture energy from the point of maximum force in the load-displacement curves. Similar average results of 2.080 ± 0.078 N/mm and 1.921 ± 0.074 N/mm were obtained from non-post cured and post cured specimens, respectively. Then, tests in low and high temperatures resulted in average G_{Ic} of 1.484 ± 0.154 N/mm and 2.854 ± 0.625 N/mm, respectively. This means a reduction of

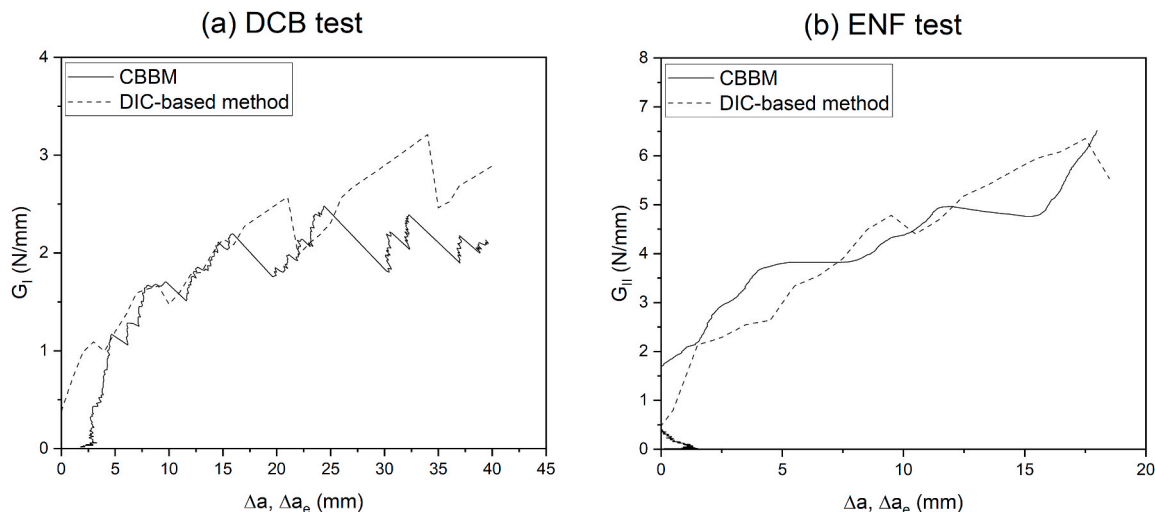


Fig. 7. Comparison between R-curves obtained with DIC crack length measurements and CBBM in (a) DCB and (b) ENF representative tests.

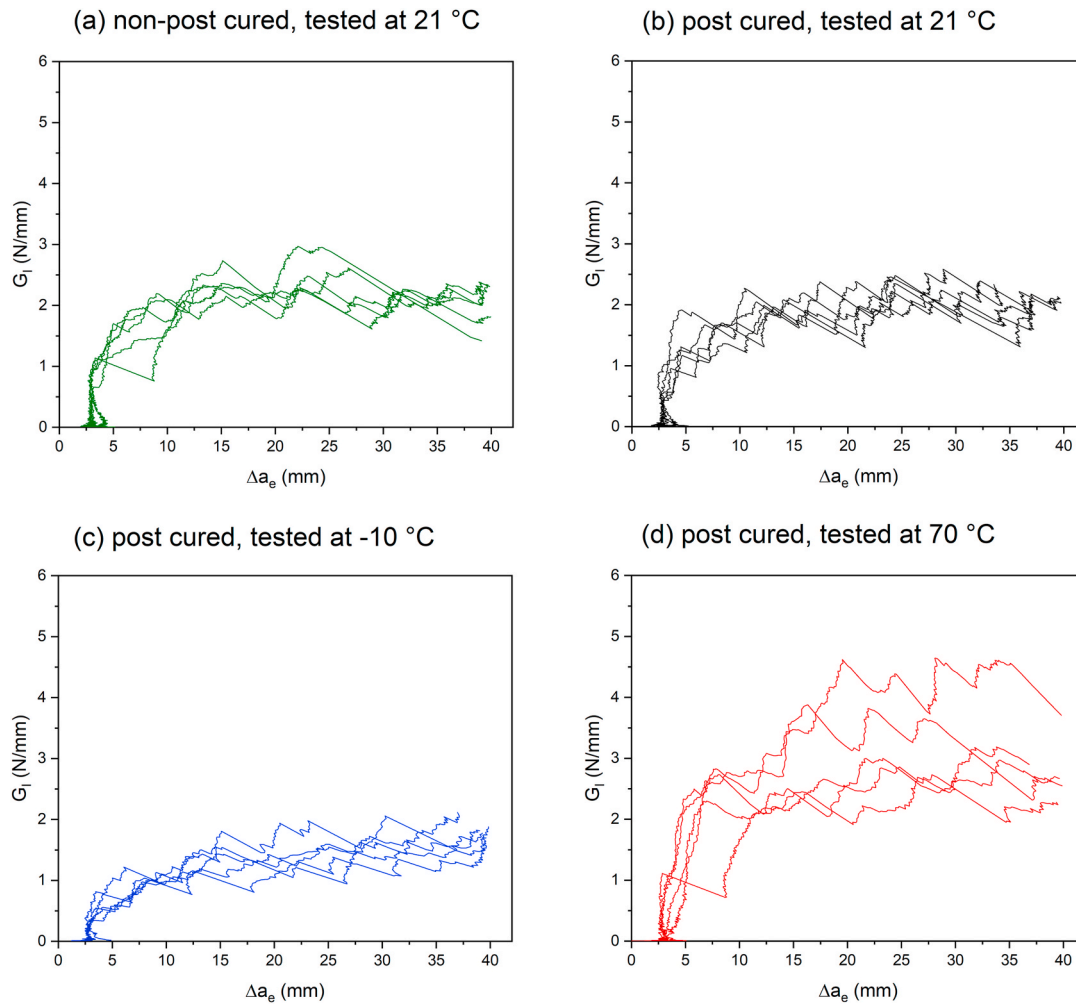


Fig. 8. Mode I R-curves from DCB tests of (a) non-post cured and (b) post cured specimens tested in room conditions, and post cured specimens tested in (c) low and (d) high temperatures.

22.8 % of the fracture toughness at $-10\text{ }^{\circ}\text{C}$ and an increase of 48.6 % at $70\text{ }^{\circ}\text{C}$. In addition, the length of the mode I FPZ was obtained from the distance between the pre-crack tip and the maximum force. The crack development of reference post cured and post cured specimen extend for an average of $7.8 \pm 2.9\text{ mm}$ and $8.7 \pm 2.9\text{ mm}$, respectively. In the case of tests in low and high temperatures, the average lengths of the FPZ are $9.9 \pm 3.7\text{ mm}$ and $8.5 \pm 2.3\text{ mm}$, respectively. A large scatter is observed due to the heterogeneity of the woven-CSM laminates.

The experimental flexural modulus was obtained from the DCB test specimens using Equation (4). Non-post cured specimens presented an average of $10.87 \pm 0.54\text{ GPa}$ and post cured reference specimens $9.28 \pm 0.79\text{ GPa}$. In addition, low and high temperature tests resulted in average flexural moduli of $10.28 \pm 1.04\text{ GPa}$, and $9.24 \pm 0.45\text{ GPa}$, respectively. Overall, no significant change in the elastic behavior of the material was observed from compliance-based measurements of DCB tests in different temperatures.

Fig. 9 shows the mode II R-curves of the ENF tests of the different testing series. Each data reduction scheme reveals an initial increase of the fracture energy followed by a short plateau region, which is subsequently followed by an increasing trend of $G_{II} = f(a)$. This effect is typical from the ENF testing method [4,8,12,22] and is explained by the local effects of compressive stresses that hinder self-similar crack propagation near the loading roller. Similarly to the mode I fracture, specimens tested in non-post cured and post cured conditions at $21\text{ }^{\circ}\text{C}$, and specimens tested at low temperature presented consistent results, as shown in Fig. 9a, b and 9c, respectively, while specimens tested in high

temperature, shown in Fig. 9d, presented more scattered results. In addition, it is important to notice that the fracture energy artificially increases at later stages of the tests due to local compression of the cracked surface near the load point.

The critical mode II fracture energy, G_{IIc} , is calculated as the fracture energy at the peak force of the ENF tests. Non-post cured and post cured specimens showed similar average results of $4.034 \pm 0.880\text{ N/mm}$ and $4.232 \pm 0.385\text{ N/mm}$, respectively. Then, tests in low and high temperatures resulted in average G_{IIc} of $3.965 \pm 0.720\text{ N/mm}$ and $5.719 \pm 0.805\text{ N/m}$, respectively. This means a reduction of 6.3 % of the fracture toughness of the composite material tested at $-10\text{ }^{\circ}\text{C}$ and an increase of 35.1 % at $70\text{ }^{\circ}\text{C}$. Additionally, the length of the mode II FPZ was determined from the distance between the pre-crack tip and the maximum force. The FPZ of reference post cured and post cured specimens extend for an average length of $5.1 \pm 4.0\text{ mm}$ and $6.8 \pm 2.6\text{ mm}$, respectively. In the case of tests in low and high temperatures, the average lengths of the FPZ are $7.6 \pm 2.6\text{ mm}$ and $6.8 \pm 1.1\text{ mm}$, respectively. Similarly to the mode I fracture, a large scatter is observed due to the heterogeneity of the woven-CSM laminates. These results show that the full crack development occurred relatively distant from the loading roller, and, therefore, is not affected by local compression.

The experimental flexural modulus was calculated from the ENF test specimens using Equation (9). Non-post cured specimens have an average of $9.55 \pm 1.10\text{ GPa}$ and post cured specimens $9.09 \pm 0.60\text{ GPa}$. There is no statistically significant difference between these results. Low temperature tests resulted in $12.50 \pm 0.34\text{ GPa}$, a significant increase of

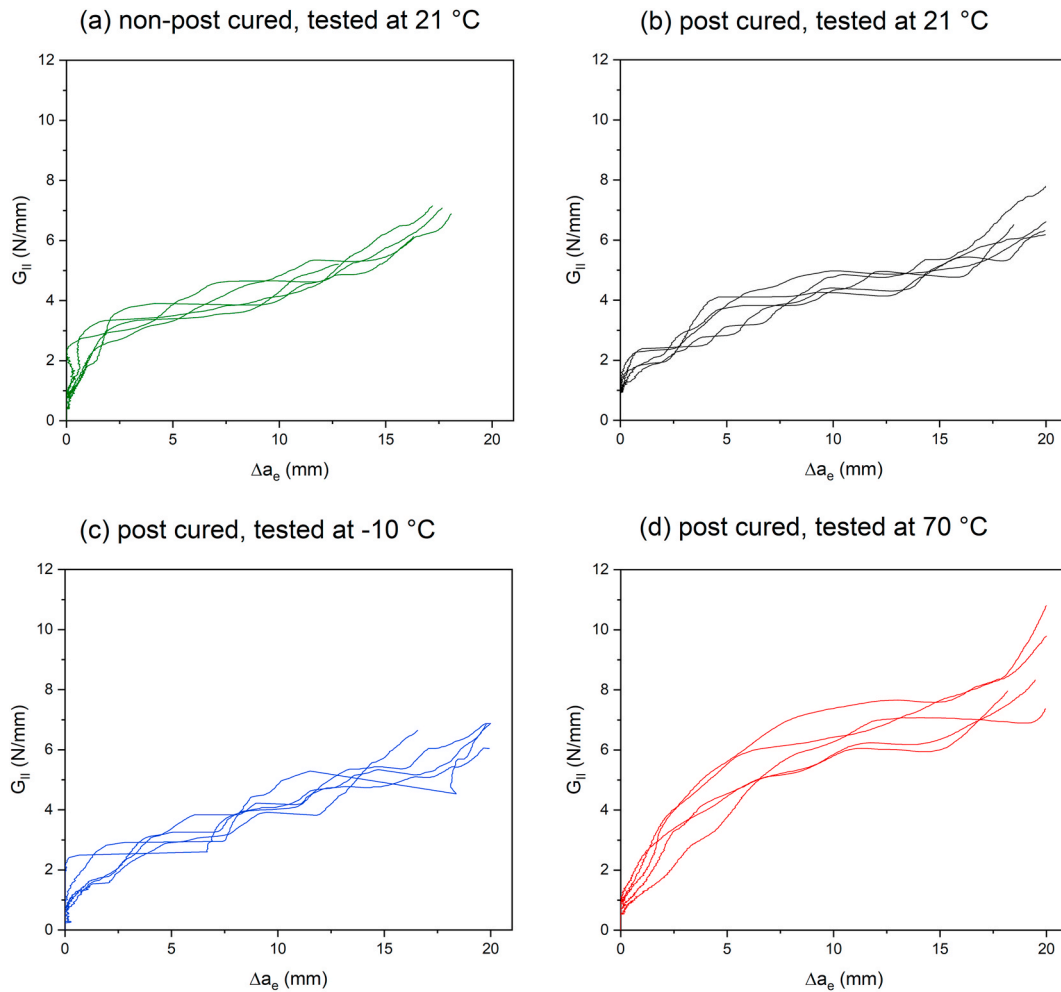


Fig. 9. Mode II R-curves from ENF tests of (a) non-post cured and (b) post cured specimens tested in room conditions, and post cured specimens tested in (c) low and (d) high temperatures.

37.6 %, and high temperature tests resulted in 7.92 ± 1.28 GPa, or a 12.9 % decrease. Overall, the ENF tests revealed a more apparent difference in the linear elastic behavior of the material in different temperatures than the DCB tests.

Results of non-post cured and post cured specimens showed consistent results in both mode I and mode II loading conditions. This confirms

that the artificial post curing of the coupon specimens does not affect the fracture behavior of the composite material. Consequently, the effect of short-term temperature changes on the fracture delamination, obtained from artificially post cured coupon specimens, can be applied to the prediction of the performance of composite structures that post cure in operational conditions. For a better visualization, Fig. 10 presents

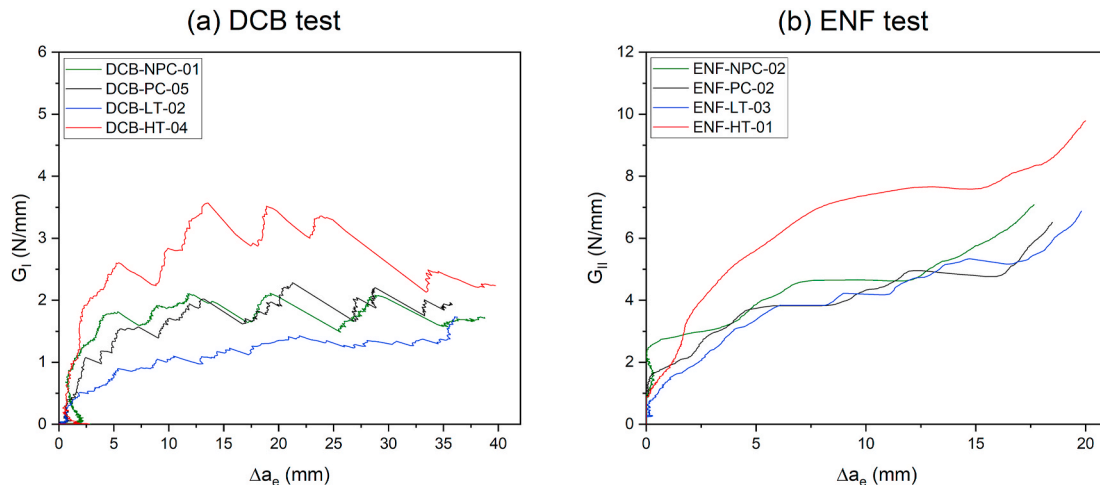


Fig. 10. Representative R-curves from (a) DCB and (b) ENF tests in different conditions.

representative mode I and mode II *R*-curves selected based on similarity of the average experimental results of critical fracture energy, length of the FPZ and flexural modulus obtained from each testing series. The short-term temperature changes showed to significantly affect the fracture toughness in both mode I and mode II loading conditions. The low temperature of $-10\text{ }^{\circ}\text{C}$ caused a significant decrease of the performance in mode I loading conditions (Fig. 10a), while the mode II fracture (Fig. 10b) showed a less apparent reduction compared to the reference testing condition of $21\text{ }^{\circ}\text{C}$. Additionally, the high temperature of $70\text{ }^{\circ}\text{C}$ resulted in an apparent increase of the material fracture performance in both mode I and mode II fracture.

4.3. Fracture surfaces

After the DCB and ENF tests, specimens were mechanically separated into two sub-laminates for visual observation of the fracture surfaces. Representative specimens were selected from each tested configuration

and high resolution images of the fracture surfaces were obtained using a 3D optical profilometer at the magnification of $\times 40$. Figs. 11 and 12 show the representative fracture surfaces from DCB and ENF tests, respectively. In addition, the height profiles of the lower fracture surfaces are displayed in Fig. 13. The measured height values were plotted with a distance of 1 mm from each other to avoid overlapping of the curves and allow comparison of the results.

The mode I fracture surfaces of non-post cured and post cured specimens (Fig. 11a and b, respectively) showed similar interlaminar failure between the CSM, on the upper surface, and the woven fiber reinforcement, on the lower surface. The concave up surface height profiles, shown in Fig. 13a, indicate an imprint of the woven surface on the CSM at the lower side of the crack. However, temperature changes showed to affect the delamination crack path of the woven-CSM composites in mode I loading conditions. Low temperature tests (Fig. 11c) resulted in a crack propagation within the CSM, which relates to a more irregular surface profile displayed in Fig. 13a. High temperature tests

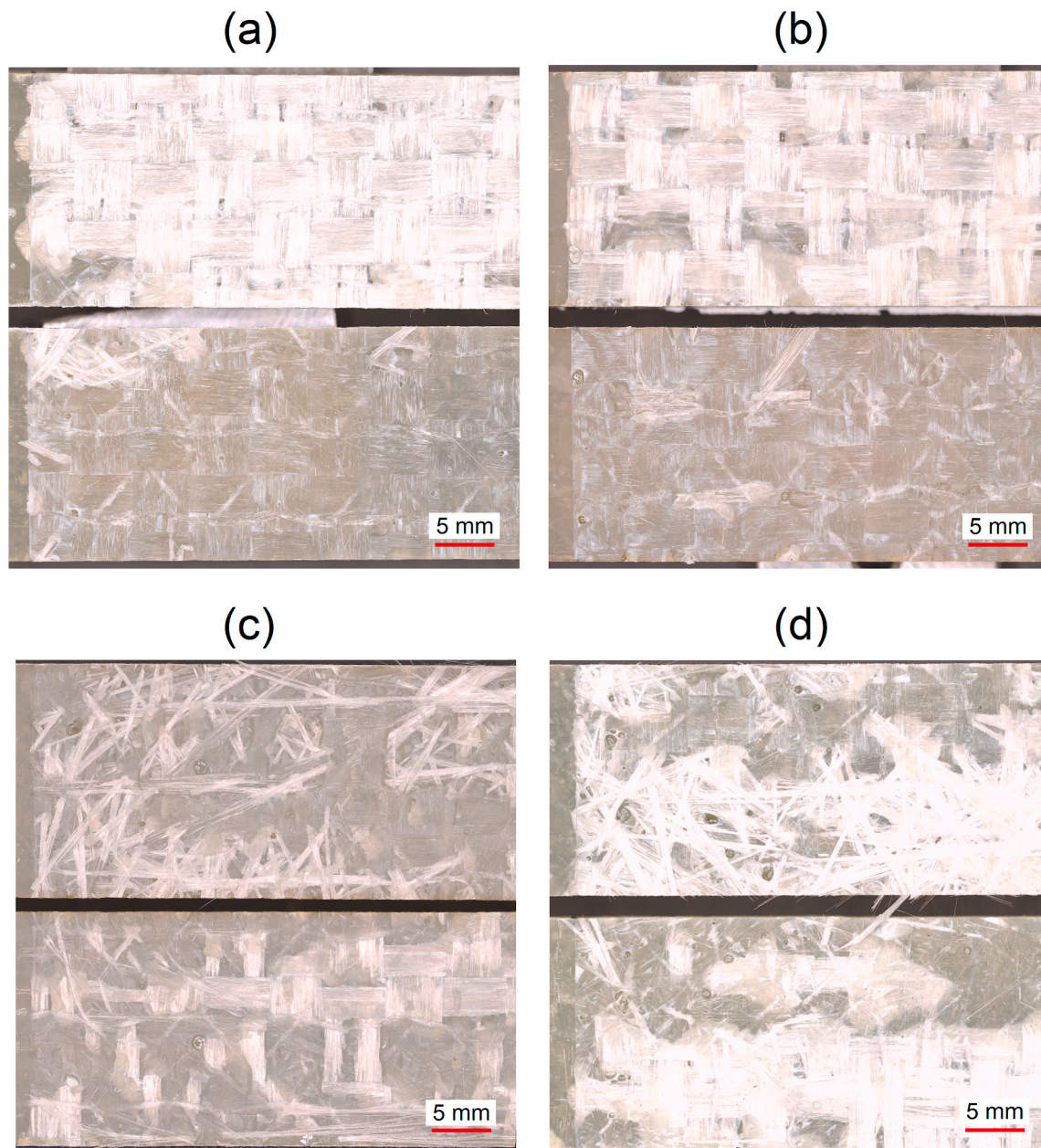


Fig. 11. Representative fracture surfaces of DCB tests from (a) non-post cured and (b) post cured specimens tested in room conditions, and post cured specimens tested in (c) low and (d) high temperatures.

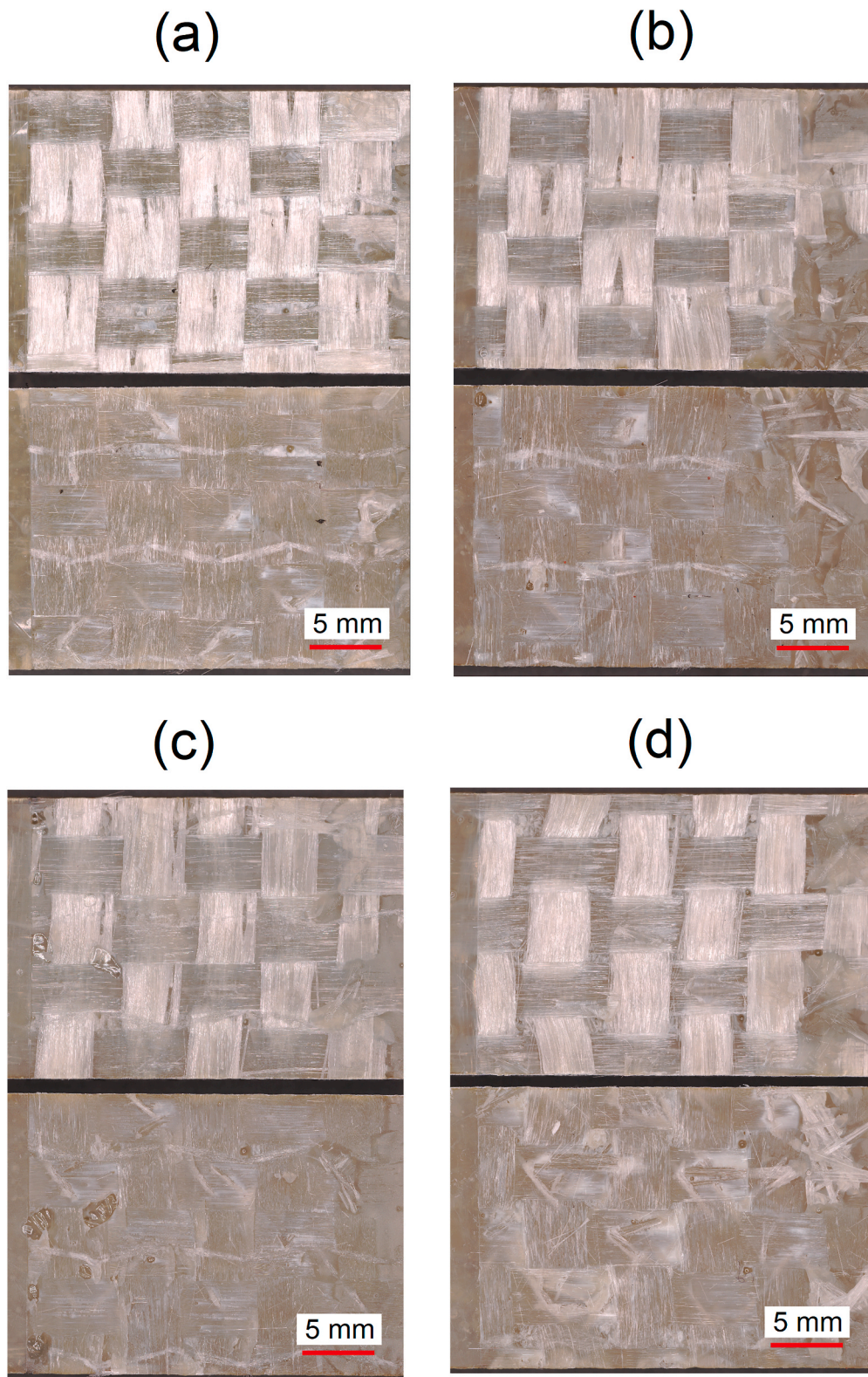


Fig. 12. Representative fracture surfaces of ENF tests from (a) non-post cured and (b) post cured specimens tested in room conditions, and post cured specimens tested in (c) low and (d) high temperatures.

showed a concave down height profile, which indicates a change of crack path with the presence of woven on the lower side of the crack. This feature is not clearly observed in the fracture surfaces (Fig. 11d).

The fracture surfaces of non-post cured and post cured specimens from mode II tests (Fig. 12a and b, respectively) showed interlaminar

failure between CSM and woven. This highlights that post curing the specimens did not affect the delamination crack path of the composite material failure mode in either mode I or mode II fracture. However, differently from the DCB tests, the crack path of ENF tests remained unaffected by temperature. Height profiles in Fig. 13b shows the same

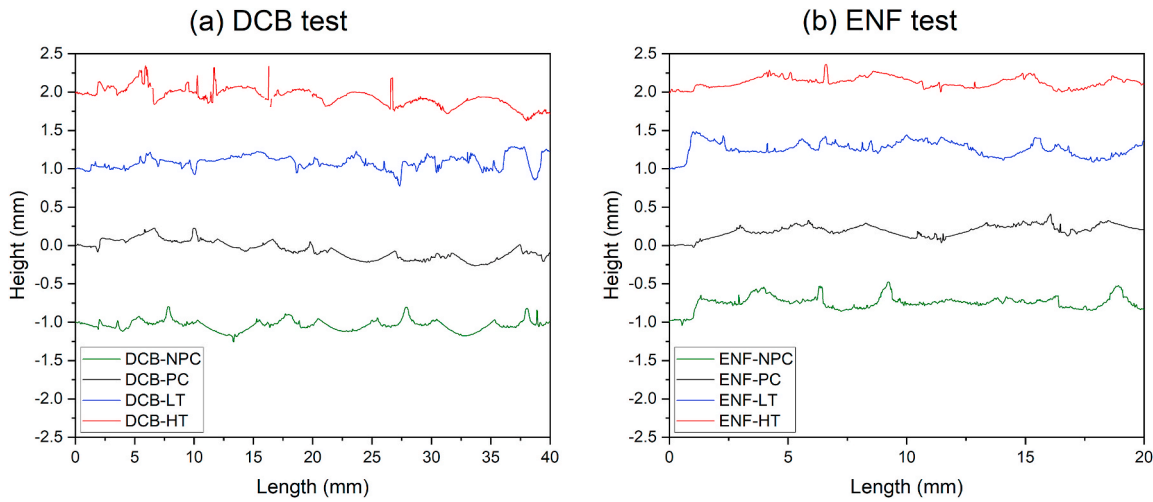


Fig. 13. Fracture surface height profiles of (a) DCB and (b) ENF tests in different conditions (absolute values shifted for comparison).

concave up curves. Overall, the measurement of fracture surface profiles showed to be an alternative solution to determine the delamination crack path of composites with complex lay-up, where visual observation and optical microscopy may not provide clear evidence.

4.4. Failure morphology

A section of the lower side of each representative specimen was

carefully cut with a handsaw for a detailed analysis of the failure modes using a scanning electron microscopy (SEM), FEI Quanta FEG 650, with a magnification of x250. Figs. 14 and 15 show the failure morphology of specimens tested in mode I and mode II fracture, respectively. Resin cusps show the deformation and cohesive failure of the matrix. Fiber imprints and bare fibers at longitudinal and transversal directions reveal woven fiber-matrix debonding. In addition, small pieces of fibers debris remained on the fracture surfaces. In mode I fracture, non-post cured

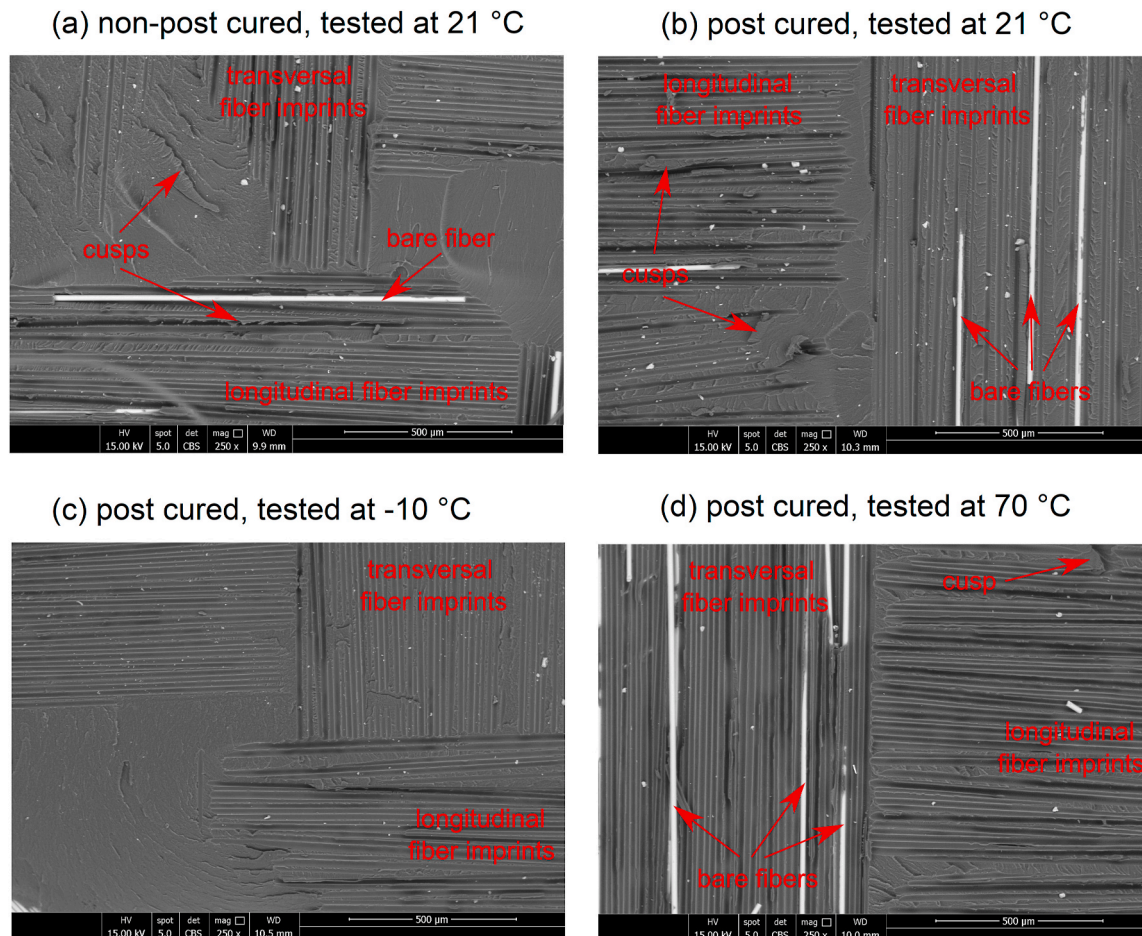


Fig. 14. Failure morphology of DCB tests (crack growth from left to right side).

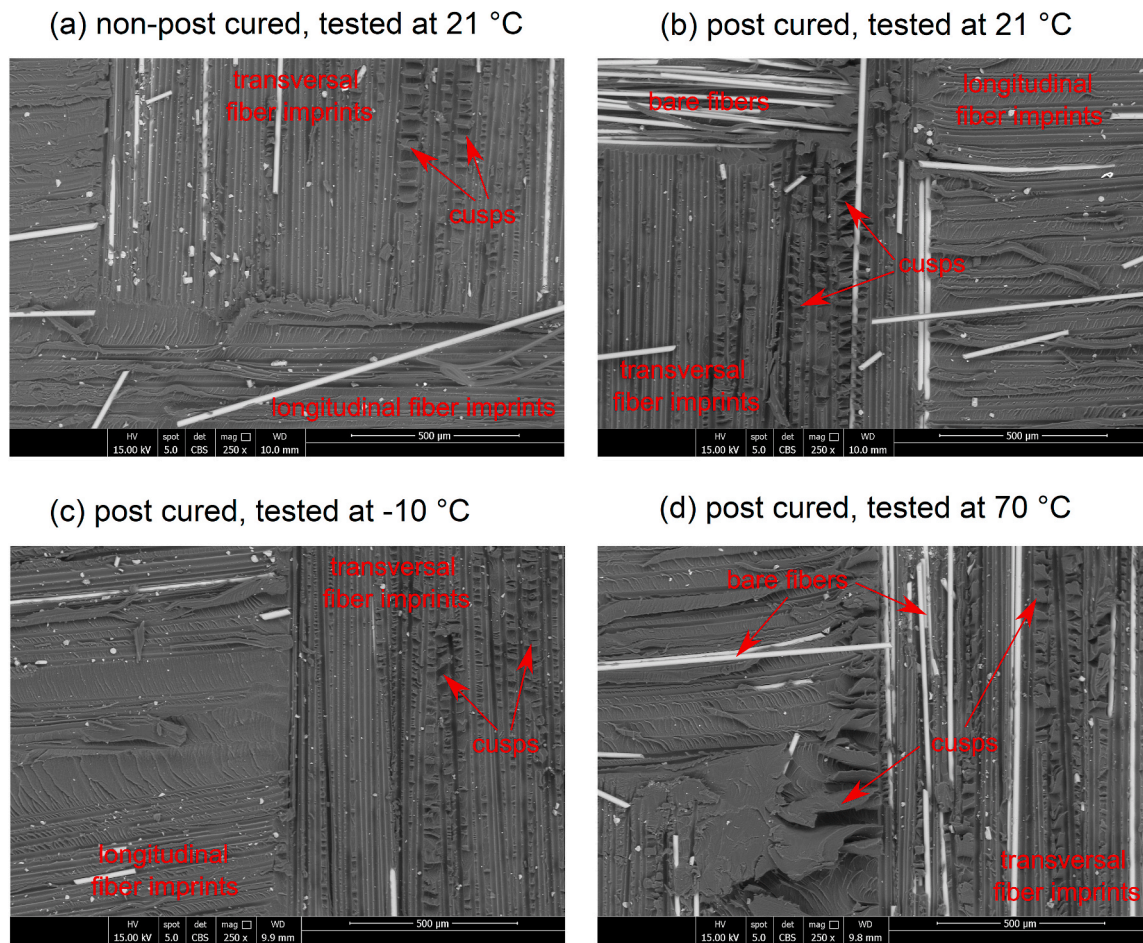


Fig. 15. Failure morphology of ENF tests (crack growth from left to right side).

(Fig. 14a) and post cured (Fig. 14b) specimens showed similar failure patterns. Low temperature tests (Fig. 14c) produced a more brittle failure, described by a flat morphology of the resin and the absence of bare fibers. This explains the reduction of the mode I fracture toughness (see Fig. 10a) in low temperature. On the other hand, high temperature tests (Fig. 14d) showed larger deformation of the resin and fracture toughness. An improvement of fiber/matrix interface adhesion is indicated by the observation of a larger matrix deformation, which contributes to a higher mode II fracture toughness.

The failure morphology of the mode II fractured non-post cured (Fig. 15a) and post cured (Fig. 15b) specimens showed similar failure patterns, such as in the case of mode I fracture. This proves that the delamination failure mode of the woven composite remains unaffected by the post curing process. The deformation of the matrix, observed by resin cusps, is typically more pronounced in shear fracture. In addition, the presence of woven fiber imprints and bare fibers is observed. No significant change is observed in low temperature tests, which agrees with the results of fracture toughness (see Fig. 10b). In the case of high temperature tests, a larger ductility of the resin is observed, which contributes to a higher fracture toughness. Overall, short-term changes of temperature affected not only the delamination crack path at macroscopic level, but also the failure morphology of the woven composite material at microscopic level.

5. Cohesive zone modelling

5.1. Cohesive behavior

A non-linear traction-separation relationship was applied to model

the cohesive behavior of a ductile interfacial fracture. It defines the global response of a cracked specimen and is divided into three stages: a linear-elastic stage ($\delta \leq \delta_e$), where δ_e is the crack opening displacement at the elastic limit; a damage evolution stage ($\delta_e < \delta \leq \delta_m$), where δ_m is the maximum relative opening displacement of the interface. In this stage, the material stiffness degenerates to 0, indicating full development of the crack and beginning of the propagation stage ($\delta > \delta_m$). Therefore, the cohesive behavior for mode I fracture can be expressed in a mathematical form:

$$\begin{cases} \sigma = \kappa\delta \rightarrow \delta \leq \delta_e \\ \sigma = \sigma(\delta) \rightarrow \delta_e < \delta \leq \delta_m \\ \sigma = 0 \rightarrow \delta > \delta_m \end{cases} \quad (12)$$

Where σ is the traction at the interface, κ is the interface stiffness in linear elastic condition, δ_e is the pre-crack tip opening displacement at crack initiation and δ_m is the pre-crack tip opening displacement at crack propagation. From this, one can derive:

$$\delta_e = \frac{\sigma_{NL}}{\kappa} \quad (13)$$

Where σ_{NL} is the traction at onset of non-linearity. The region along the crack path between the root of the crack and the point of crack propagation (complete degradation of interface stiffness) is the FPZ, and can be modelled by a cohesive behavior between two predefined surfaces. Therefore, the relationship between the mode I fracture energy (G_I) and the crack tip opening displacement (δ_I) defines the cohesive model, as follows:

$$G_I = \int \sigma(\delta_I) d\delta_I \tag{14}$$

Equation (14) correlates the experimental mode I fracture energy (G_I), calculated from the CBBM (see section 3), and the crack tip opening displacements (δ_I) 4.3. As such, it allows obtaining the mode I traction-separation relationship assigned to the cohesive behavior by applying the derivative with respect to δ_I on both sides of the integral function. Analogously, the mode II fracture can be modelled using G_{II} and the crack tip slip displacements (δ_{II}).

5.2. Crack tip opening and slip displacements

The crack tip opening displacement (CTOD) was obtained by DIC of the representative DCB tests at the section of the pre-crack tip. The CTOD is determined by the relative vertical displacements between the upper and lower sides of the crack, as shown in Fig. 5a. The results are not sensitive to the location where the points are extracted in the DIC images. In the case of mode II fracture, the crack tip slip displacement (CTSD) is obtained from the relative longitudinal displacements at the section of the pre-crack tip, as shown in Fig. 16. The CTSD is determined by the distance between the linear extrapolation of the longitudinal displacement of the lower and upper arms of the crack in the height of the crack. The contribution of specimen rotation to the CTSD is negligible. Moreover, the DIC image of the specimen exhibits a concentration of the shear strain (ϵ_{xy}) ahead of the pre-crack tip, indicating the formation of a FPZ during the tests.

Results from representative DCB tests are shown in Fig. 17a. The curves is determined by several CTOD points obtained from DIC until the critical point of crack propagation, which is determined based on the plateau of the fracture energy (see R-curves in Fig. 7). The mode I critical

fracture energy (G_{Ic}) of the representative DCB tests are 2.11 N/mm in room temperature, 1.33 N/mm in low temperature, and 3.08 N/mm in high temperature. A fitting curve was created to describe the development of G in function of δ . For consistency of the analysis, the curve fitting procedure is the same in each testing condition (reference post cured, low temperature and high temperature).

The traction-separation curves that define the mode I cohesive behavior of the woven laminate are presented in Fig. 17b. A sharp decrease of traction is observed in initial stages, followed by an extensive region of low traction. These curves show typical shapes of a mode I traction-separation relationship [6] with extensive fibre bridging. The most relevant change occurred between 0.0 and 0.5 mm of crack opening displacement. For better visualization, Fig. 17c shows the detail of the cohesive behavior in the first 0.2 mm of crack opening. The early stages of crack development are generally related to the cohesive failure of the resin matrix. As observed in Fig. 14, the failure morphology of the matrix changed from a more brittle behavior in low temperature to a more ductile failure in high temperature. This effect of temperature on the mode I composite delamination reappears in the derived cohesive model for specimens tested at high temperature. However, no significant change is noticed at later stages of crack tip damage development, after 0.5 mm of crack opening. This indicates that the average fiber bridging effects of the woven laminate is insensitive to temperature changes.

An analogous approach, owing to the derivation of Eq. (14), was applied to obtain the mode II associated traction-separation curves by pairing the CTSD 4.3 to the R-curves from ENF tests. Such as in the DCB tests, the amount of points extracted from the ENF tests and the type of curve fitting have minor effect on the shape of the derived cohesive behavior. The results from representative ENF tests are shown in Fig. 18a. The mode II critical fracture energy (G_{IIc}) are 4.94 N/mm in

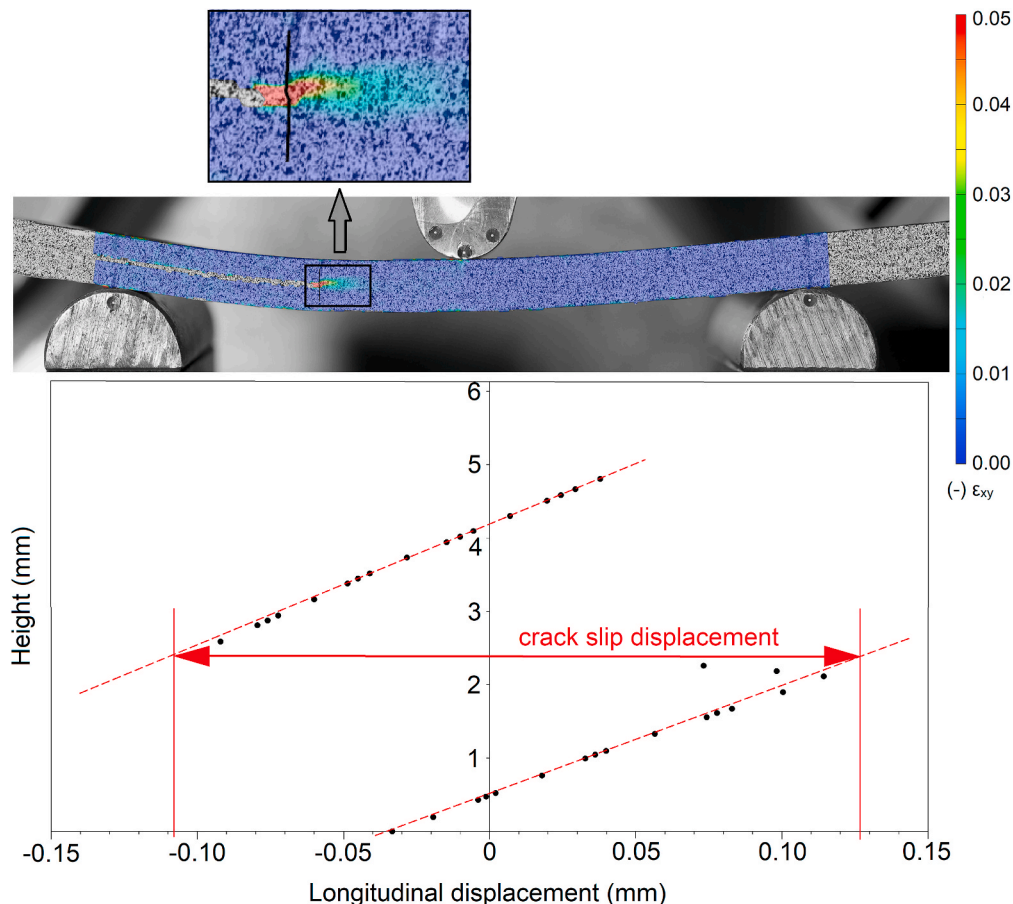


Fig. 16. Pre-crack tip slip displacement measured with DIC from the section of initial crack tip during ENF tests.

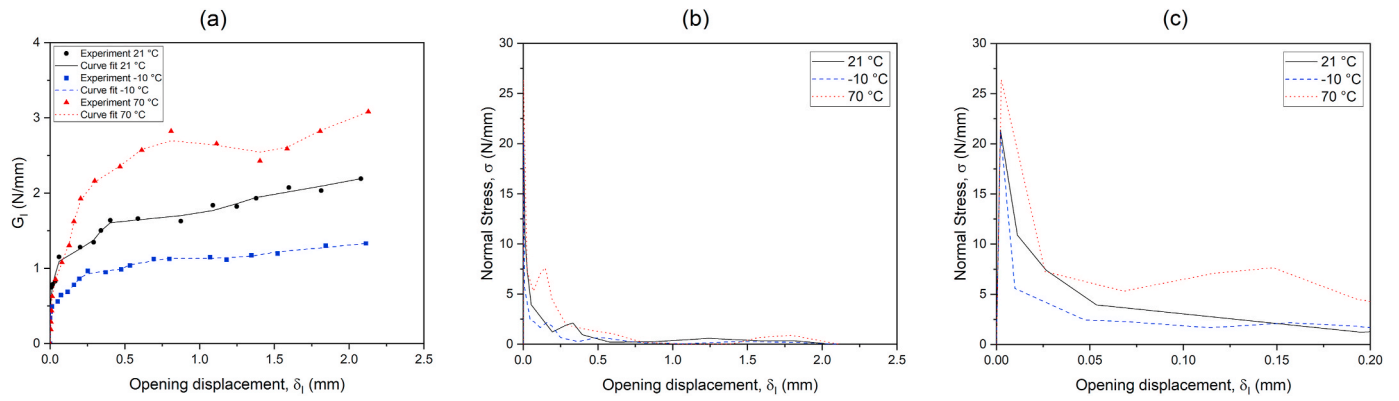


Fig. 17. Mode I (a) experimental fracture and (b) cohesive behavior with (c) detail of the first 0.2 mm of crack opening.

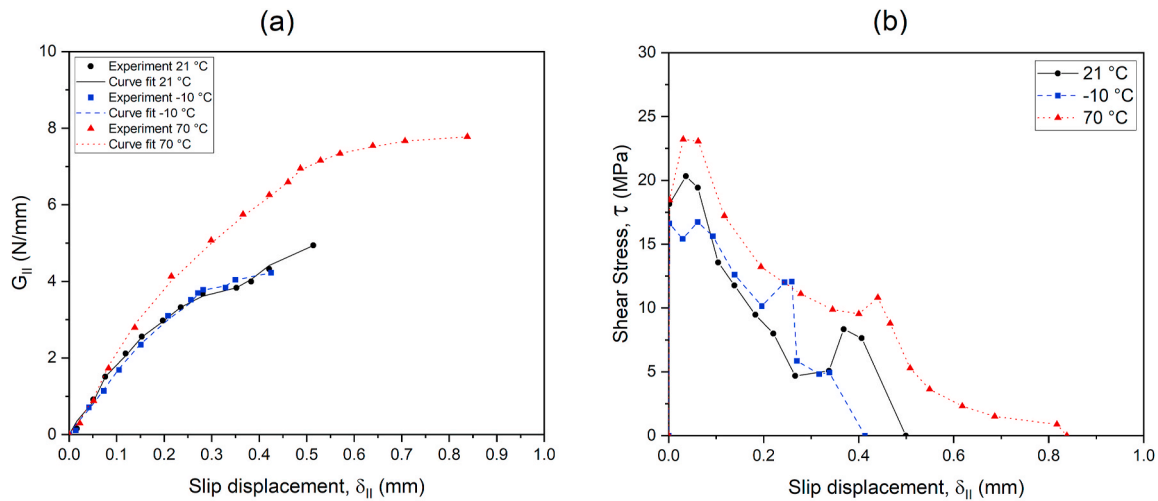


Fig. 18. Mode II (a) experimental fracture and (b) cohesive behavior.

room temperature, 4.23 N/mm in low temperature, and 7.78 N/mm in high temperature.

The traction-separation curves that define the mode II delamination are presented in Fig. 18b. It is noticed that the increase of temperature increased the maximum traction (shear stress) estimated at early stages of the crack development (between 0.0 and 0.1 mm slip displacement) from 16 MPa in -10°C , to 20 MPa in 21°C , and 23 MPa in 70°C . Similar behavior was found by Ref. [19] using a trapezoidal cohesive law. In the initial stages of damage process (up to 0.3 mm of CTSD), tests in room and low temperatures showed similar cohesive behavior (see Fig. 18b). However, high temperature produced significant larger CTSD. The ultimate slip displacement increased from 0.5 mm in room temperature to over 0.8 mm in high temperature. These changes in the mode II cohesive model can be correlated to the increased plastic deformation of the resin identified in Fig. 15b and d. An increase in ductility of the woven composite delamination occurred in high temperature compared to the other conditions of shear fracture.

5.3. Finite element models

The DCB and ENF tests were implemented in FEM using Abaqus/Explicit solver. A tridimensional geometry of each model was based in the actual representative specimens and test set up. The woven-CSM composite laminate was modelled as a homogeneous material divided in two equal sub-laminates with a midplane contact interface. Geometry and boundary conditions can be found in Fig. 19a, for the DCB, and Fig. 19b, for the ENF test models. The composite specimen was meshed

with solid 4-node linear tetrahedron elements. In the ENF test models, the loading and support rollers were modelled as deformable 4-node shell elements with reduced integration, hourglass control and finite membrane strains.

An orthotropic elastic material was defined for the composite material in the finite element model. Table 2 shows the material properties used in the models. The longitudinal elastic modulus (E_{11}) is the most relevant material property that affects the global response of the test models. Therefore, these parameters were taken from experiments to account for the effect of temperature changes on the mechanical behavior. The input values of E_{11} (and consequently E_{22}) were assumed the same as the E_f obtained from Equation (4), for DCB test models, and Equation (9), for ENF test models. Nominal values were used for the remaining elastic properties based on previous works [27,32]. Typical steel isotropic properties ($E = 210\text{ GPa}$ and $\nu = 0.3$) were applied to the loading and support rollers of the ENF tests. A preliminary analysis showed that stresses in the specimen are significantly lower than the strength of the material and plasticity does not affect the mechanical response of the models.

A general contact interaction was defined with hard contact and penetration-based formulation for the normal behavior. In addition, a tangential isotropic friction coefficient of 0.1 was imposed for all candidate contact pair surfaces in the model, such as the pre-cracked surfaces, and the specimen contact with support and loading rollers in the ENF test model. The interface interaction was modelled using cohesive behavior. The linear interface stiffness (κ) is a numerical parameter, and its value within a reasonable range has a negligible

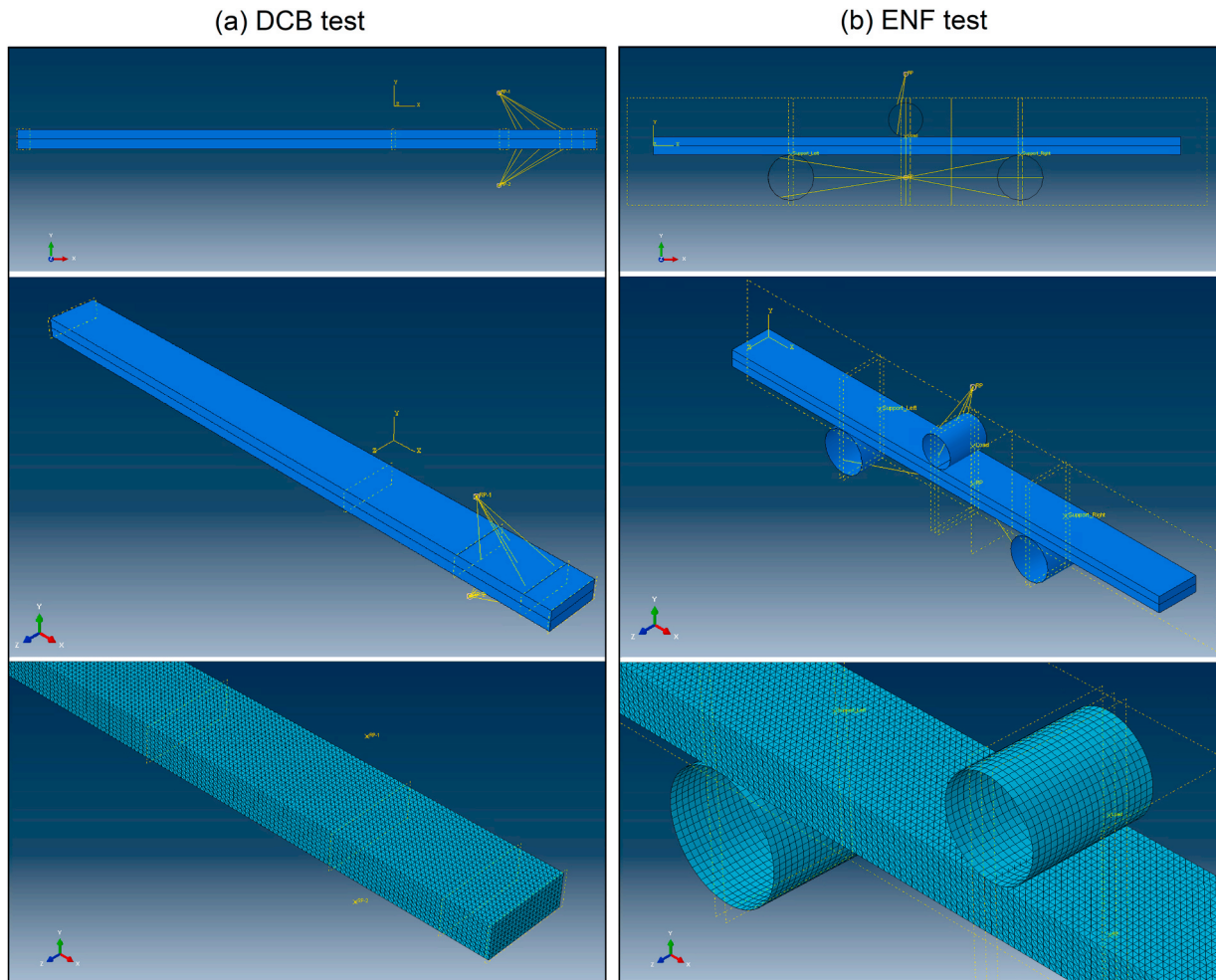


Fig. 19. Finite element models of the (a) DCB and (b) ENF tests.

Table 2
Orthotropic material properties used in the models.

Elastic property	Value
$E_{11}; E_{22}$	E_f from experiment
E_{33}	5.0 GPa
G_{12}	3.1 GPa
$G_{13}; G_{23}$	3.5 GPa
ν_{12}	0.35
$\nu_{13}; \nu_{23}$	0.30

influence on the computational results [33]. A maximum nominal stress of 2 MPa was defined for the damage initiation of each fracture mode (G_I , G_{II} and G_{III}), and the damage evolution was determined directly from the traction-separation points obtained from the experiments (see Figs. 17b and 18b for mode I and mode II fracture, respectively). The consistency of the element size was verified based on the convergence of the load response during the displacement-driven simulation of the test. An optimal element size was achieved using a global mesh of 1.0 mm elements and a minimum of 4 elements through the thickness of each sub-laminate. Detailed images of the mesh are can be seen in Fig. 19.

5.4. Mechanical response

Load-displacement curves were extracted from the finite element models of representative DCB and ENF tests at reference (21 °C), low (−10 °C) and high (70 °C) temperatures. The mechanical response of numerical models is compared to experimental results in Fig. 20. Results

of the DCB tests (Fig. 20a) show that the numerical load-displacement responses match well until the maximum load is reached. This shows that the pure mode I crack initiation is accurately predicted using CZM directly modelled in this work. After the maximum load, numerical results presented relatively smoother curves that remain between the peaks and valleys of the experimental results. In fact, the cohesive behavior is modelled from the region of crack formation, which leads to an averaged mechanical response observed during crack propagation. This fiber bridging effect tends to diminish as the size increases from relatively small standard coupons to larger structures.

Results of the ENF tests (Fig. 20b) showed good agreement between experiments and numerical models. The conformity of stiffnesses in the linear elastic stage of the tests shows that the material properties were accurately modelled by compliance-based estimations in each temperature. This is more noticeable in low temperature tests. Since there is no obvious effect of fiber bridging in mode II tests, numerical load-displacement curves showed good agreement with experiments. Overall, the cohesive models derived directly from experimental results were capable of accurately predicting the delamination fracture behavior of the composite material in different temperatures in both mode I and mode II loading conditions. These interlaminar fracture properties can be applied to the design of structural components with complex geometries.

6. Conclusion

This work addressed the effect of short-term changes of temperature

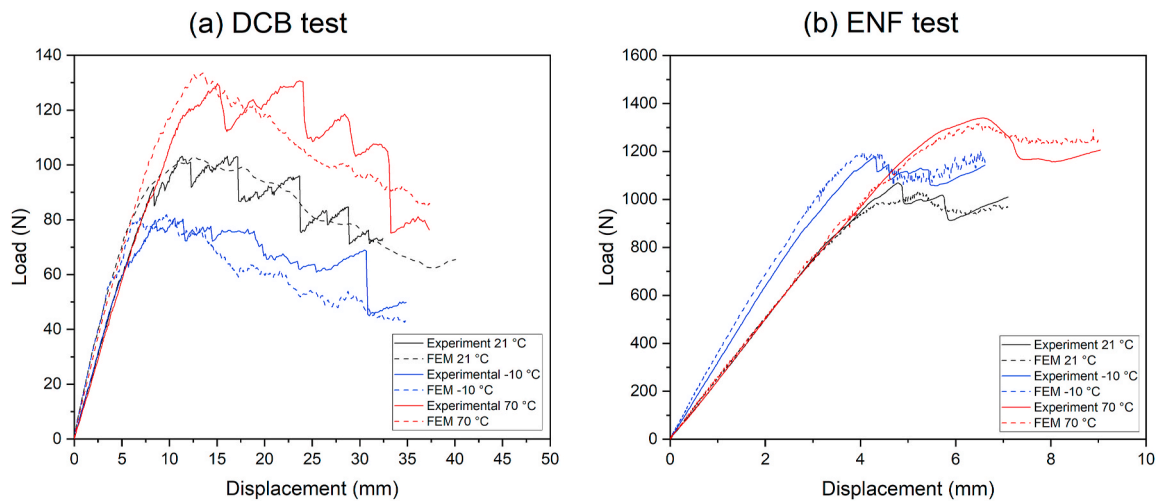


Fig. 20. Representative experimental and numerical load-displacement curves of the (a) DCB and (b) ENF tests.

on the delamination fracture behavior of a glass fiber woven composite laminate interleaved with chopped strand mat (CSM). Mode I and mode II loading conditions were considered using DCB and ENF tests. Non-post cured and post cured specimens were tested at room temperature (21 °C), and post cured specimens were tested at -10 and 70 °C. The material behavior was investigated using analytical and numerical methods, and the following conclusions were obtained.

- The analytical compliance-based beam method (CBBM) provided reliable fracture toughness and R -curves of the woven-CSM laminate when compared to the results obtained from direct measurements of the crack length using DIC;
- Temperature changes affect the preferential crack path for the woven composite delamination in mode I loading conditions. Similar crack paths occurred in low (-10 °C) and room (21 °C) temperatures occurred preferentially between the woven and CSM, while in high temperature (70 °C) the crack progressed more within the layer of CSM. However, the crack path in mode II fracture tests remained independent of the testing temperature;
- Temperature affected not only the delamination crack path at macroscopic level, but also the failure morphology of the composite material at microscopic level. Fractography images revealed a transition in the failure mechanism at higher temperatures to more fiber/matrix interface debonding and matrix deformation, which induced a denser fiber bridging mechanism with larger crack opening/shear displacements and larger FPZ. The increase of matrix ductility translated into larger amplitudes of the R -curves with an improvement of the delamination fracture toughness in both mode I and mode II loading conditions;
- A comparison between non-post cured and post cured specimens showed consistent mechanical behavior and failure mechanisms. This proved that the post curing process did not affect the delamination performance of the investigated woven glass fiber and vinyl ester based composite material even though remarkably distinct glass transition temperatures were observed;
- Non-linear cohesive models were directly derived from experiments with DIC measurements of crack tip displacements. The obtained traction-separation curves successfully described the changes in crack development at different temperatures both in mode I and mode II fracture. Results were used in numerical simulations of the DCB and ENF tests to accurately reproduce the experimental load-displacement responses at different temperatures.

CRediT authorship contribution statement

Marcio Moreira Arouche: Writing – original draft, Visualization, Validation, Methodology, Investigation, Formal analysis, Conceptualization. **Marko Pavlovic:** Writing – review & editing, Supervision, Funding acquisition.

Declaration of competing interest

The authors declare the following financial interests/personal relationships which may be considered as potential competing interests: Marcio Moreira Arouche reports financial support was provided by Netherlands Enterprise Agency. If there are other authors, they declare that they have no known competing financial interests or personal relationships that could have appeared to influence the work reported in this paper.

Acknowledgments

The authors would like to express their gratitude to RVO for the financial support with Topsector Energie subsidie van het Ministerie van Economische Zaken through WrapNode-I and WrapNode-II projects, and Tree Composites B.V. for the production of specimens.

Data availability

Data will be made available on request.

References

- [1] Budhe S, et al. An updated review of adhesively bonded joints in composite materials. *Int J Adhesion Adhes* 2017;72:30–42.
- [2] Chaves FJP, et al. Fracture mechanics tests in adhesively bonded joints: a literature review. *J Adhes* 2014;90(12):955–92.
- [3] de Moura MFSF, Morais JLL, Dourado N. A new data reduction scheme for mode I wood fracture characterization using the double cantilever beam test. *Eng Fract Mech* 2008;75(13):3852–65.
- [4] de Moura MFSF, Campilho RDSG, Gonçalves JPM. Pure mode II fracture characterization of composite bonded joints. *Int J Solid Struct* 2009;46(6): 1589–95.
- [5] Pereira FAM, et al. Direct and inverse methods applied to the determination of mode I cohesive law of bovine cortical bone using the DCB test. *Int J Solid Struct* 2017;128:210–20.
- [6] Huo X, et al. On characterization of cohesive zone model (CZM) based upon digital image correlation (DIC) method. *Int J Mech Sci* 2022;215:106921.
- [7] Gorman JM, Thouless MD. The use of digital-image correlation to investigate the cohesive zone in a double-cantilever beam, with comparisons to numerical and analytical models. *J Mech Phys Solid* 2019;123:315–31.
- [8] Azevedo JCS, et al. Cohesive law estimation of adhesive joints in mode II condition. *Theor Appl Fract Mech* 2015;80:143–54.

- [9] Ouyang Z, Li G. Nonlinear interface shear fracture of end notched flexure specimens. *Int J Solid Struct* 2009;46(13):2659–68.
- [10] Fernandes RMRP, et al. Determination of cohesive laws of composite bonded joints under mode II loading. *Compos B Eng* 2013;52:269–74.
- [11] Moreira Arouche M, Teixeira de Freitas S, de Barros S. On the influence of glass fiber mat on the mixed-mode fracture of composite-to-metal bonded joints. *Compos Struct* 2021;256:113109.
- [12] De Baere J, et al. Study of the Mode I and Mode II interlaminar behaviour of a carbon fabric reinforced thermoplastic. *Polym Test* 2012;31(2):322–32.
- [13] Höwer D, et al. Experimental and numerical investigation of the mixed mode delamination of monolithic laminates exhibiting severe fiber bridging. *Compos Struct* 2020;242:112035.
- [14] Sela N, Ishai O, Banks-Sills L. The effect of adhesive thickness on interlaminar fracture toughness of interleaved cfrp specimens. *Composites* 1989;20(3):257–64.
- [15] Saghafi H, et al. The effect of interleaved composite nanofibrous mats on delamination behavior of polymeric composite materials. *Compos Struct* 2014;109:41–7.
- [16] Zheng N, et al. Improvement of interlaminar fracture toughness in carbon fiber/epoxy composites with carbon nanotubes/polysulfone interleaves. *Compos Sci Technol* 2017;140:8–15.
- [17] Idrees M, Palmese GR, Alvarez NJ. Maximizing the interlaminar fracture toughness of thermoset interleaved woven glass fiber laminates. *Compos Appl Sci Manuf* 2023;172:107616.
- [18] Hosseini MR, Taheri-Behrooz F, Salamat-talab M. Mode II interlaminar fracture toughness of woven E-glass/epoxy composites in the presence of mat interleaves. *Int J Adhesion Adhes* 2020;98:102523.
- [19] Fernandes RL, de Moura MFSF, Moreira RDF. Effect of temperature on pure modes I and II fracture behavior of composite bonded joints. *Compos B Eng* 2016;96:35–44.
- [20] Ibrahim GR, Albarbar A. A new approach to the cohesive zone model that includes thermal effects. *Compos B Eng* 2019;167:370–6.
- [21] Cao J, et al. On temperature-dependent fiber bridging in mode I delamination of unidirectional composite laminates. *Compos Appl Sci Manuf* 2023;171:107581.
- [22] Machado JJM, et al. Mode II fracture toughness of CFRP as a function of temperature and strain rate. *Compos B Eng* 2017;114:311–8.
- [23] Reed RP, Golda M. Cryogenic properties of unidirectional composites. *Cryogenics* 1994;34(11):909–28.
- [24] Mohammadi B, et al. A new FE modeling procedure to investigate the effects of toughening mechanisms on the fracture toughness of laminated composites. *Theor Appl Fract Mech* 2020;107:102507.
- [25] Mivehchi H, Varvani-Farahani A. The effect of temperature on fatigue strength and cumulative fatigue damage of FRP composites. *Procedia Eng* 2010;2(1):2011–20.
- [26] He P, Pavlovic M. Failure modes of bonded wrapped composite joints for steel circular hollow sections in ultimate load experiments. *Eng Struct* 2022;254:113799.
- [27] Feng W, Arouche MM, Pavlovic M. Influence of surface roughness on the mode II fracture toughness and fatigue resistance of bonded composite-to-steel joints. *Construct Build Mater* 2024;411:134358.
- [28] ISO 6721. Plastics — determination of dynamic mechanical properties — Part 11: glass transition temperature. International Organization for Standardization; 2019.
- [29] ASTM D5528/D5528M. Standard test method for mode I interlaminar fracture toughness of unidirectional fiber-reinforced polymer matrix composites. ASTM International; 2021.
- [30] ASTM D7905/D7905M. Standard test method for determination of the mode II interlaminar fracture toughness of unidirectional fiber-reinforced polymer matrix composites. ASTM International; 2019.
- [31] Hashemi S, et al. The analysis of interlaminar fracture in uniaxial fibre-polymer composites. *Proce. Royal Soc. London. A. Mathe. Phys. Sci.* 1990;427(1872):173–99.
- [32] He P, et al. Mode I fracture behavior of glass fiber composite-steel bonded interface – experiments and CZM. *Compos Struct* 2024;330:117814.
- [33] Lu X, et al. On cohesive element parameters and delamination modelling. *Eng Fract Mech* 2019;206:278–96.